



**HAL**  
open science

## **N-Iodosaccharin–pyridine co-crystal system under pressure: experimental evidence of reversible twinning**

Vishnu Vijayakumar-Syamala, Emmanuel Aubert, Maxime Deutsch, Emmanuel Wenger, Arun Dhaka, Marc Fourmigué, Massimo Nespolo, Enrique Espinosa

### ► To cite this version:

Vishnu Vijayakumar-Syamala, Emmanuel Aubert, Maxime Deutsch, Emmanuel Wenger, Arun Dhaka, et al.. N-Iodosaccharin–pyridine co-crystal system under pressure: experimental evidence of reversible twinning. *Acta Crystallographica Section B: Structural Science, Crystal Engineering and Materials* [2014-..], 2022, 78, pp.436 - 449. 10.1107/s2052520622002542 . hal-03688876

**HAL Id: hal-03688876**

**<https://hal.univ-lorraine.fr/hal-03688876>**

Submitted on 6 Jun 2022

**HAL** is a multi-disciplinary open access archive for the deposit and dissemination of scientific research documents, whether they are published or not. The documents may come from teaching and research institutions in France or abroad, or from public or private research centers.

L'archive ouverte pluridisciplinaire **HAL**, est destinée au dépôt et à la diffusion de documents scientifiques de niveau recherche, publiés ou non, émanant des établissements d'enseignement et de recherche français ou étrangers, des laboratoires publics ou privés.



## ***N*-Iodosaccharin–pyridine co-crystal system under pressure: experimental evidence of reversible twinning**

**Vishnu Vijayakumar-Syamala, Emmanuel Aubert, Maxime Deutsch,  
Emmanuel Wenger, Arun Dhaka, Marc Fourmigué, Massimo Nespolo and  
Enrique Espinosa**

*Acta Cryst.* (2022). **B78**, 436–449



**IUCr Journals**

CRYSTALLOGRAPHY JOURNALS ONLINE

Author(s) of this article may load this reprint on their own web site or institutional repository provided that this cover page is retained. Republication of this article or its storage in electronic databases other than as specified above is not permitted without prior permission in writing from the IUCr.

For further information see <https://journals.iucr.org/services/authorrights.html>



# *N*-Iodosaccharin–pyridine co-crystal system under pressure: experimental evidence of reversible twinning

Vishnu Vijayakumar-Syamala,<sup>a</sup> Emmanuel Aubert,<sup>a</sup> Maxime Deutsch,<sup>a</sup> Emmanuel Wenger,<sup>a</sup> Arun Dhaka,<sup>b</sup> Marc Fourmigué,<sup>b</sup> Massimo Nespolo<sup>a</sup> and Enrique Espinosa<sup>a\*</sup>

Received 18 October 2021

Accepted 4 March 2022

<sup>a</sup>Universite de Lorraine, CNRS, CRM2, Nancy, France, and <sup>b</sup>Universite de Rennes I, CNRS, ISCR (Institut des Sciences Chimiques de Rennes) UMR 6226, Rennes 35042, France. \*Correspondence e-mail: enrique.espinosa@univ-lorraine.fr

Edited by C. M. Reddy, IISER Kolkata, India

**Keywords:** intermolecular interactions; high-pressure studies; single-crystal X-ray diffraction; twinning.

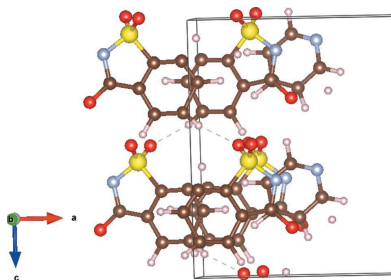
**CCDC references:** 2156534; 2156535; 2156536; 2156537; 2156538; 2156539; 2156540; 2156541; 2156542; 2156543; 2156544; 2156545; 2156546; 2156547; 2156548; 2156549; 2156550; 2156551; 2156552

**Supporting information:** this article has supporting information at journals.iucr.org/b

This work presents a single-crystal X-ray diffraction study of an organic co-crystal composed of *N*-iodosaccharin and pyridine (NISac-py) under hydrostatic pressure ranging from 0.00 (5) GPa to 4.5 (2) GPa. NISac-py crystallizes in the monoclinic system (space group  $B2_1/e$ ). The unconventional setting of the space group is adopted (the conventional setting is  $P2_1/c$ , No. 14) to emphasise the strongly pseudo-orthorhombic symmetry of the lattice, with a  $\beta$  angle very close to  $90^\circ$ . The crystal structure contains one molecule each of *N*-iodosaccharin (NISac) and pyridine (py) in the asymmetric unit ( $Z' = 1$ ), linked via an  $N_{\text{sac}} \cdots I \cdots N'_{\text{py}}$  halogen-bonding motif. A gradual modification of this motif is observed under pressure as a result of changes in the crystalline environment. Mechanical twinning is observed under compression and the sample splits into two domains, spanning an unequal volume that is mapped by a twofold rotation about the  $[100]$  direction of the  $B2_1/e$  unit cell. The twinning is particularly significant at high pressure, being reversible when the pressure is released. The structure of the twinned sample reveals the continuity of a substantial substructure across the composition plane. The presence of this common substructure in the two orientations of the twinned individuals can be interpreted as a structural reason for the formation of the twin and is the first observed example in a molecular crystal. These results indicate that the anisotropy of intermolecular interactions in the crystal structure results in an anisotropic strain generated upon the action of hydrostatic compression. Periodic density functional theory calculations were carried out by considering an isotropic external pressure, the results showing good agreement with the experimental findings. The bulk modulus of the crystal was obtained from the equations of state, being 7 (1) GPa for experimental data and 6.8 (5) GPa for theoretical data.

## 1. Introduction

Control of the structure and properties of crystalline solids is one of the most important aims in the field of crystal engineering. The physico-chemical properties of a molecular crystal are due not only to the properties of its molecular components, but also to their specific assembly. Clear evidence of this feature is offered by the phenomenon of polymorphism, where different spatial arrangements of the same molecule lead not only to obviously new crystal structures but also to different thermodynamic properties (Brog *et al.*, 2013). Another possibility to modify the properties of a given compound in its solid phase is to undertake its co-crystallization with other molecules, also called co-formers. This strategy allows modification of the properties of the solid,



which becomes a multicomponent system or a co-crystal. Accordingly, through co-crystallization, new supramolecular structures involving different intermolecular patterns bring modifications in the properties of the parent solid. In the literature we find a large number of studies dealing with this kind of research, taking advantage of the large area opened by multicomponent systems (Tiekink & Zukerman-Schpector, 2017).

The molecular environment can also be modified by applying an external constraint on the crystal structure, such as a variation in temperature or pressure. Thus, with the exception of negative thermal expansion (NTE) materials, lowering the temperature usually induces shrinking of the crystal structure, a consequence of the variation in the relative positions of the molecules in space as they approach each other. Pressure is less commonly exploited as a means of adjusting the physico-chemical properties of a crystal, due to the intrinsic experimental limitations. Nonetheless, today high-pressure research on organic crystals is a well established field and a hot topic of interest among different research communities, because pressure can act as another thermodynamic variable that allows alteration of the structure, inducing significant modifications of non-covalent intermolecular interactions. These changes are much more pronounced than those obtained by modifying the temperature. In most of the studies involving organic crystals under pressure, an anisotropic strain is generated upon the action of external pressure, resulting in different compressibilities along each crystallographic direction and making the analysis of non-covalent intermolecular interactions significant (Boldyreva *et al.*, 2005; Orgzall *et al.*, 2008). As the system attempts to minimize the interaction between closely approaching molecules, this anisotropy can also sometimes trigger a phase transition at a certain pressure (Giordano *et al.*, 2019).

Hydrogen bonding is a major class of non-covalent interactions that has been studied in detail under high pressure.

Since the initial studies dealing with hydrogen bonding in oxalic acid (Putkonen *et al.*, 1985) several reports have been published, illustrating the sensitivity of hydrogen-bonding networks to high pressure (Yan *et al.*, 2012; Mishra *et al.*, 2020). Analogous to hydrogen bonding, halogen bonding is another class of non-covalent interactions widely exploited by the crystal engineering community (Desiraju *et al.*, 2013; Cavallo *et al.*, 2016). Halogen bonding has been less well explored than hydrogen bonding by the high-pressure community, even though it could also potentially show significant variations in intermolecular distances and angles under high pressure.

In this study we present the crystal structure analysis of an organic co-crystal composed of *N*-iodosaccharin and pyridine (NISac-py) under variable pressure ranging from 0.00 (5) GPa to 4.5 (2) GPa. In the asymmetric unit, the parent components are linked via an  $N_{\text{sac}} \cdots I \cdots N'_{\text{py}}$  halogen-bonding motif (termed  $N1 \cdots I1 \cdots N2$ , based on the atom-numbering scheme), where the  $\sigma$ -hole of iodine (belonging to the NISac molecule) acts as the electrostatic positive region of the halogen-bonding donor, and the lone pair of  $N'_{\text{py}}$  acts as the negative electrostatic region of the halogen-bonding acceptor [Fig. 1(a), and Fig. S6 in the supporting information]. In this work, modifications of the pointed halogen-bonding motif have been studied in detail as a function of pressure. The crystal structure of the same NISac-py system was reported previously (Dolenc & Modec, 2009), but the moderate quality of the sample did not allow those researchers to obtain a satisfactory structural model (the  $R_1$  and  $wR_2$  agreement factors were 0.0879 and 0.2702, respectively), as stated by the authors. Later, another attempt was made by Makhotkina *et al.* (2015), but the structural solution was not accomplished due to the complex diffraction pattern measured. In the current study, we have obtained a good structural model for NISac-py at room temperature [ $T = 298$  (5) K] and low temperature [ $T = 100$  (2) K], both at ambient pressure. In addition, high-pressure X-ray diffraction (HPXRD) experiments were carried out using a membrane diamond anvil cell

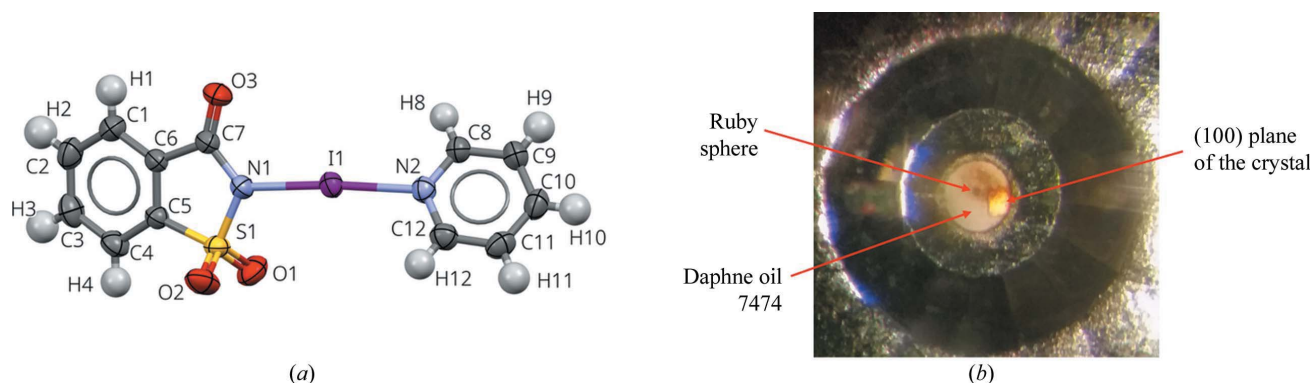


**Figure 1**

(a) The molecular structure of the NISac-py complex formed by the  $N_{\text{sac}} \cdots I \cdots N'_{\text{py}}$  halogen-bonding motif in the co-crystal (termed  $N1 \cdots I1 \cdots N2$ , based on the atom-numbering scheme given in the figure). Displacement ellipsoids are drawn at the 50% probability level, and H atoms are shown as small spheres of arbitrary radii. (b) An NISac-py single crystal mounted inside the MDAC sample chamber with the cell axis quasi-perpendicular to the (100) plane of the crystal (space group setting  $B2_1/e$ ). A ruby sphere ( $\sim 10$   $\mu\text{m}$  in radius) is placed in the middle of the sample chamber for pressure calibration. The sample chamber is filled with Daphne oil 7474 as the pressure-transmitting medium.

(MDAC) in a setup developed in our laboratory and adapted to the diffractometer (Bruker D8 Venture). In a compression–decompression cycle of pressure, a reversible mechanical twinning was observed. The structure of the twinned sample was then investigated in terms of the pseudo-eigensymmetry of the crystallographic orbits (Marzouki *et al.*, 2014a), revealing the continuity of a substantial substructure across the composition plane. In the past, the presence of a common substructure in the two orientations of twinned individuals has been confirmed in several examples of mineral structures (*e.g.* Marzouki *et al.*, 2014a,b, 2015), being interpreted as a structural reason for the formation of the twin. To the best of our knowledge, however, this is the first example in a molecular crystal.

## 2. Experimental

### 2.1. MDAC loading and centring

A 1:1 stoichiometric co-crystal of *N*-iodosaccharin and pyridine (NISac·py) was prepared by slow solvent evaporation from ethyl acetate solution (for more details see the supporting information). Crystals of dimensions  $0.149 \times 0.122 \times 0.053$  mm (crystal 1) and  $0.110 \times 0.091 \times 0.048$  mm (crystal 2) were chosen carefully with the aid of a polarized light microscope (for more details see the supporting information) for crystal structure determination at, respectively, ambient pressure (room and low temperature) and high pressure (room temperature). Crystal 2 is smaller than crystal 1 (used for data collection under ambient conditions) because it needs to fit within the MDAC sample chamber. Crystal 2 was thus placed inside this chamber, with the pressure-cell axis quasi-perpendicular to the (100) face of the crystal (for more details see the supporting information). A ruby sphere of  $\sim 10$   $\mu$ m diameter was placed inside the sample chamber for *in situ* measurement of the pressure by the ruby luminescence (PRL) technique (Piermarini *et al.*, 1975), while Daphne oil 7474 (Murata *et al.*, 2008) was used as the pressure-transmitting medium [Fig. 1(b)]. The initial sealing of the cell does not cause any measurable change in pressure, being thus similar to ambient pressure. The MDAC was then mounted on an in-house developed goniometer head [Fig. S1(a)]. For the HPXRD experiments, a Bruker D8 Venture diffractometer was used. Optical centring perpendicular to the MDAC axis was done using the camera of the PRL device in combination with the camera of the diffractometer, while the centring along the MDAC axis was performed according to the procedure described by Dawson *et al.* (2004). Hydrostatic pressures ranging from 0.00 (5) GPa to 4.5 (2) GPa were applied in a sequential manner, first increasing, and then decreasing to ambient pressure. The force was applied to the MDAC by means of a membrane inflated with helium gas, using a pneumatic drive system connected through a metallic capillary [Fig. S1(b)]. The pressure inside the cell was monitored via the PRL device fixed directly on the base of the goniometer using an aluminium rail [Fig. S1(c)]. The MDAC is equipped with a micro-valve [Fig. S1(a)], allowing

disconnection of the pneumatic drive system once the target pressure is reached. The MDAC can therefore be oriented in all directions on the diffractometer without any capillary winding problem.

### 2.2. Single crystal X-ray diffraction

**2.2.1. Data collection under ambient conditions, processing and refinement.** X-ray diffraction data were collected for crystal 1 at room temperature and ambient pressure using a Bruker D8 Venture diffractometer, equipped with a molybdenum micro-focus X-ray tube (Mo  $K\alpha$  radiation,  $\lambda = 0.71073$  Å) with mirror optics as a monochromator and a PHOTON III CMOS detector of size  $10 \times 14$  cm. Data integration and reduction were carried out using the *SAINTE* program incorporated in the *APEX3* software (Bruker, 2019). A numerical absorption correction was applied using the crystal shape and face indexing. The crystal structure was solved using the *SHELXT* (Sheldrick, 2015a) program and refined using the *SHELXL* (Sheldrick, 2008, 2015b) program in the *OLEX2-1.3* suite (Dolomanov *et al.*, 2009). All the non-hydrogen atoms were refined anisotropically. H atoms were placed at calculated positions and constrained to ride on their parent atoms [Fig. 2(a)]. The crystallographic information is gathered in Table S1. Crystal structure analysis was carried out using the *OLEX2-1.3* and *CrystalExplorer* (Version 17.5) (Turner *et al.*, 2017) software packages. Crystal structure drawings were prepared using *Mercury* (Version 2020.1) (Macrae *et al.*, 2020).

**2.2.2. Data collection at high pressure and room temperature, processing and refinement.** X-ray diffraction data were collected under pressure ranging from 0.00 (5) GPa to

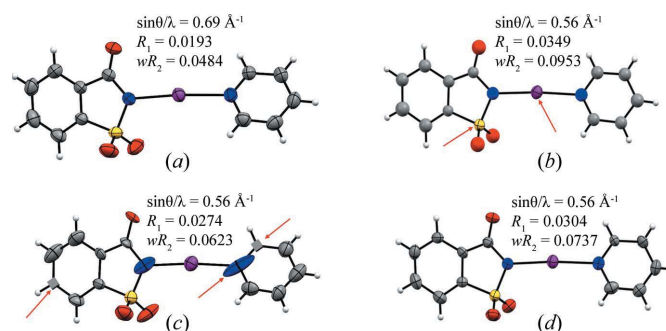


**Figure 2**

(a) The structural model determined under ambient conditions (outside the MDAC). (b) The structural model determined with data collected with the crystal inside the MDAC at 0.5 (1) GPa and at room temperature, in which only the I and S atoms (indicated with red arrows) have been refined with anisotropic displacement parameters (ADPs). (c) Anisotropic refinement of other non-hydrogen atoms for the structural model determined with the crystal inside the MDAC, with red arrows showing unrealistic (deformed ellipsoids) and physically meaningless (cube representation in the convention of *Mercury* software) ADPs of atoms. (d) The structural model determined after transferring the ADPs from the model under ambient conditions, with proper scaling. The maximum resolution limit and agreement factors ( $R_1$  and  $wR_2$ ) corresponding to each model are shown at the top of the respective figures.

4.5 (2) GPa at room temperature, using the same Bruker D8 Venture diffractometer equipped with a molybdenum micro-focus X-ray tube (Mo  $K\alpha$  radiation,  $\lambda = 0.71073 \text{ \AA}$ ) with mirror optics as a monochromator, and a PHOTON III CMOS detector of size  $10 \times 14 \text{ cm}$ . Here, a short collimator and long beam stop are used to be consistent with the size of the pressure cell. Data integration and reduction were carried out using *SAINTE* after excluding the shadowed regions with a dynamic mask (Bruker, 2019; Dawson *et al.*, 2004). A half-aperture angle of  $40^\circ$  and a  $\varphi$  offset of  $-4^\circ$  were used in the DAC section of the integration interface of the software. An empirical absorption correction based on the intensities using *SADABS* (Krause *et al.*, 2015) was used. The atomic coordinates of the structure determined under ambient conditions were used as the starting model for the refinement of the crystal structure with data collected at the first pressure measured inside the MDAC, corresponding to 0.00 (5) GPa. For all the data sets, only the heavier atoms (I1 and S1) could be refined anisotropically [Fig. 2(b)]. Attempts to refine all other non-hydrogen atoms anisotropically resulted in non-positive definite (or unrealistic) anisotropic displacement parameters (ADPs) [Fig. 2(c)] as a consequence of hidden reciprocal-space zones and therefore of missing information in the measured data sets (completeness is only  $\sim 40\%$  up to a resolution of  $0.56 \text{ \AA}^{-1}$ ). To retrieve a good structural model, ADPs for all other non-hydrogen atoms were transferred from the structural model under ambient conditions (crystal 2), assuming that pressure affects  $U_{ij}$  in a similar way to  $U_{\text{iso}}$ . Hence, ADPs used for crystal structure determination (with data sets collected from the crystal inside the MDAC) were calculated as  $(U_{ij})_{\text{in},PX} = K \times (U_{ij})_{\text{out},P0}$ , where the scale factor  $K = (U_{\text{iso}})_{\text{in},PX} / (U_{\text{iso}})_{\text{in},P0}$  is obtained for each pressure  $X$ . [The values of  $(U_{ij})_{\text{out},P0}$  correspond to ADPs obtained from the data set collected with no MDAC under ambient conditions, while  $(U_{\text{iso}})_{\text{in},P0}$  and  $(U_{\text{iso}})_{\text{in},PX}$  correspond to isotropic displacement parameters obtained from data sets collected with the crystal inside the MDAC at  $P = 0$  and  $P = X$ , respectively.]

Once determined, the  $(U_{ij})_{\text{in},PX}$  ADPs were kept fixed and not refined further, leading to improvement in the refinement parameters in the final model [Fig. 2(d)]. H atoms were placed at calculated positions and constrained to ride on their parent atoms. Additionally, SADI (same distance) restraints (with a standard deviation value of  $0.02 \text{ \AA}$ ) were applied to the aryl ring of NISac and to the pyridine ring to keep their distortions as small as possible. The structural model obtained at 0.00 (5) GPa was used as the initial reference model for further refinements with high-pressure data sets. Additional information for the high-pressure crystal structures can be found in Tables 1 and 2.

It should be noted here that the  $(U_{ij})_{\text{out},P0}$  ADPs used in this procedure were those obtained from crystal 2 (namely, the crystal retrieved after the HPXRD experiments and subjected to data collection outside the MDAC under ambient conditions) rather than from crystal 1 outside the MDAC. The crystallographic information corresponding to crystal 2 under ambient conditions can be found in Table S2.

### 3. DFT calculations

#### 3.1. Periodic plane wave calculations

The crystal structure of NISac-py was optimized as a function of isotropic pressure using the *CASTEP* software (Version 19.11; Clark *et al.*, 2005). The experimental structure determined under ambient conditions in the  $P2_1/a$  setting of the space group [Dolenc & Modec, 2009; Cambridge Structural Database (CSD; Groom *et al.*, 2016) refcode MUGDAU,  $a = 12.6184 (3) \text{ \AA}$ ,  $b = 7.8019 (2) \text{ \AA}$ ,  $c = 14.8718 (4) \text{ \AA}$ ,  $\beta = 113.6530 (12)^\circ$ ] was used as the starting point, and optimizations were performed from  $-0.25 \text{ GPa}$  to  $4.5 \text{ GPa}$  in  $0.25 \text{ GPa}$  increments. All atomic positions were allowed to vary, together with the cell parameters, while keeping the monoclinic symmetry. The PBE exchange and correlation functional was used, complemented by semi-empirical dispersion corrections (Grimme, 2006). A fine plane wave cut off was used, corresponding to a limit of  $625 \text{ eV}$ . The MP grid size was set to  $4 \times 4 \times 4$ . The optimization convergence criteria were fixed as follows: maximal stress tolerance at convergence  $0.1 \text{ GPa}$ , energy shift  $1 \times 10^{-5} \text{ eV}$ , force  $5 \times 10^{-2} \text{ a.u.}$ , displacement  $1 \times 10^{-3} \text{ \AA}$ . Subsequent analyses on the theoretical data set were performed after transformation of the obtained crystal structures from the  $P2_1/a$  setting to the  $B2_1/e$  setting of the space group. Table S3 shows the unit-cell parameters and volume as a function of pressure, along with unit-cell void volumes calculated with the *ASV* program (Petitjean, 1994).

#### 3.2. Isolated molecule calculations

Density functional theory (DFT) calculations were performed on the isolated NISac-py adduct, and on NISac and py molecules extracted from the crystal structure determined under ambient conditions. Intramolecular C–H bond distances were normalized to standard neutron distances and no geometry optimizations were done. Single-point calculations were performed using the *GAUSSIAN09* software (Frisch *et al.*, 2013) and the B3LYP functional, completed with dispersion corrections (Grimme *et al.*, 2010). The Def2TZVP basis set was employed for all atoms, including a pseudo-potential for iodine (Pritchard *et al.*, 2019). The *AIMAll* software (Keith, 2019) was then used to calculate atomic charges (Table S4).

#### 3.3. Intermolecular interaction energy decomposition

*CrystalExplorer* (Version 17.5; Turner *et al.*, 2017) was used to calculate intermolecular interaction energies and their decompositions into electrostatic, polarization, dispersion and repulsive terms, employing the B3LYP functional and the DGDZVP basis set for all atoms. Intramolecular C–H bond distances were normalized to standard neutron distances.

## 4. Results

Suitable crystals of NISac-py were grown as described in Section 2.1 and Section S1. With the aid of a polarized light microscope, the best crystals were selected for the X-ray

**Table 1**

Crystallographic information for data collected with increasing pressure.

For all data sets: space group setting  $B2_1/e$  (unconventional setting of  $P2_1/c$ , No. 14),  $Z = 8$ ,  $T = 298$  (5) K, formula weight  $388.17 \text{ g mol}^{-1}$ , crystal size  $0.110 \times 0.091 \times 0.048 \text{ mm}$ , radiation type Mo  $K\alpha$ , number of parameters 71 and number of restraints 18. The parameter  $S$  is the goodness of fit, GoF.

	Pressure (GPa)								
	0.00 (5)	0.20 (5)	0.4 (1)	0.5 (1)	0.9 (1)	1.5 (2)	2.0 (2)	3.3 (2)	4.5 (2)
$a$ (Å)	27.291 (14)	27.185 (16)	27.108 (16)	26.998 (13)	26.806 (12)	26.653 (12)	26.559 (12)	26.304 (11)	26.020 (12)
$b$ (Å)	7.8228 (16)	7.7444 (19)	7.6595 (19)	7.5869 (15)	7.4450 (14)	7.3257 (13)	7.2336 (13)	7.0512 (11)	6.9618 (13)
$c$ (Å)	12.628 (3)	12.593 (3)	12.539 (3)	12.485 (3)	12.380 (2)	12.284 (2)	12.209 (2)	12.042 (2)	11.937 (2)
$\beta$ (°)	88.579 (11)	88.608 (12)	88.662 (13)	88.802 (11)	89.057 (10)	89.236 (10)	89.462 (9)	89.932 (9)	89.476 (10)
Volume (Å <sup>3</sup> )	2695.1 (16)	2650.4 (18)	2602.9 (18)	2556.7 (14)	2470.4 (13)	2398.2 (12)	2345.4 (12)	2233.5 (11)	2162.3 (11)
$\mu$ (mm <sup>-1</sup> )	2.54	2.58	2.63	2.67	2.77	2.85	2.91	3.06	3.16
$T_{\text{min}}, T_{\text{max}}$	0.461, 0.563	0.445, 0.563	0.394, 0.563	0.456, 0.563	0.451, 0.563	0.455, 0.563	0.467, 0.563	0.472, 0.562	0.502, 0.563
No. of measured, independent and observed [ $I > 2\sigma(I)$ ] reflections	10351, 770, 595	9901, 777, 564	8139, 761, 536	9824, 738, 577	9464, 706, 573	9116, 688, 582	8817, 675, 580	8569, 656, 590	7793, 635, 553
$R_{\text{int}}$	0.045	0.071	0.080	0.054	0.046	0.044	0.046	0.040	0.046
$\theta_{\text{max}}$ (°)	23.2	23.3	23.2	23.3	23.2	23.3	23.3	23.2	23.4
$(\sin \theta/\lambda)_{\text{max}}$ (Å <sup>-1</sup> )	0.555	0.555	0.555	0.556	0.555	0.555	0.556	0.554	0.559
$R [F^2 > 2\sigma(F^2)]$ , $wR (F^2)$ , $S$	0.030, 0.080, 1.05	0.036, 0.096, 1.07	0.038, 0.109, 1.17	0.034, 0.091, 1.15	0.033, 0.090, 1.16	0.037, 0.095, 1.13	0.042, 0.107, 1.19	0.020, 0.038, 1.12	0.029, 0.049, 1.20
$\Delta\rho_{\text{max}}, \Delta\rho_{\text{min}}$ (e Å <sup>-3</sup> )	0.46, -0.34	0.39, -0.47	0.51, -0.48	0.53, -0.43	0.82, -0.43	0.85, -0.44	0.70, -0.41	0.22, -0.22	0.29, -0.31
BASF† (%)	0.15 (5)	0.15 (6)	0.21 (7)	0.19 (6)	0.23 (7)	0.61 (10)	2.30 (18)	15.02 (9)	14.48 (13)
Obliquity $\omega$ (°)	1.42	1.39	1.34	1.20	0.94	0.76	0.54	0.07	0.52

† BASF(%) corresponds to the batch scale factor parameter obtained after the final refinement cycle, indicating the percentage of domain 2 in the structure.

**Table 2**

Crystallographic information for data collected with decreasing pressure.

For all data sets: space group setting  $B2_1/e$  (unconventional setting of  $P2_1/c$ , No. 14),  $Z = 8$ ,  $T = 298$  (5) K, formula weight  $388.17 \text{ g mol}^{-1}$ , crystal size  $0.110 \times 0.091 \times 0.048 \text{ mm}$ , radiation type Mo  $K\alpha$ , number of parameters 71 and number of restraints 18. The parameter  $S$  is the goodness of fit, GoF.

	Pressure (GPa)							
	2.4 (2)	1.9 (2)	1.3 (2)	0.8 (1)	0.5 (1)	0.05 (5)	0.00 (5)	
$a$ (Å)	26.482 (12)	26.581 (13)	26.742 (14)	26.869 (13)	27.035 (13)	27.246 (16)	27.272 (19)	
$b$ (Å)	7.1755 (13)	7.2485 (14)	7.3842 (15)	7.4985 (14)	7.6231 (15)	7.819 (2)	7.834 (2)	
$c$ (Å)	12.156 (2)	12.220 (2)	12.337 (3)	12.418 (3)	12.507 (3)	12.621 (3)	12.630 (4)	
$\beta$ (°)	89.626 (10)	89.447 (10)	89.154 (11)	88.952 (10)	88.799 (11)	88.538 (13)	88.507 (15)	
Volume (Å <sup>3</sup> )	2309.9 (12)	2354.4 (13)	2436.0 (15)	2501.5 (14)	2577.1 (14)	2687.7 (19)	2697 (2)	
$\mu$ (mm <sup>-1</sup> )	2.96	2.90	2.81	2.73	2.65	2.54	2.53	
$T_{\text{min}}, T_{\text{max}}$	0.485, 0.563	0.490, 0.563	0.488, 0.563	0.479, 0.563	0.486, 0.563	0.470, 0.563	0.470, 0.563	
No. of measured, independent and observed [ $I > 2\sigma(I)$ ] reflections	8506, 673, 590	8768, 687, 590	8933, 712, 582	9489, 759, 603	9685, 773, 603	10196, 817, 583	8714, 830, 545	
$R_{\text{int}}$	0.046	0.047	0.053	0.049	0.053	0.063	0.069	
$\theta_{\text{max}}$ (°)	23.3	23.2	23.3	23.2	23.2	23.3	23.2	
$(\sin \theta/\lambda)_{\text{max}}$ (Å <sup>-1</sup> )	0.556	0.555	0.556	0.555	0.555	0.555	0.555	
$R [F^2 > 2\sigma(F^2)]$ , $wR (F^2)$ , $S$	0.037, 0.083, 1.15	0.042, 0.102, 1.17	0.043, 0.109, 1.14	0.037, 0.101, 1.14	0.039, 0.100, 1.15	0.041, 0.103, 1.08	0.040, 0.113, 1.08	
$\Delta\rho_{\text{max}}, \Delta\rho_{\text{min}}$ (e Å <sup>-3</sup> )	0.34, -0.33	0.81, -0.43	0.72, -0.41	0.82, -0.49	0.54, -0.39	0.45, -0.37	0.38, -0.51	
BASF† (%)	8.8 (2)	2.89 (18)	1.00 (14)	0.27 (7)	0.09 (6)	0.16 (8)	0.05 (7)	
Obliquity $\omega$ (°)	0.37	0.55	0.85	1.05	1.20	1.46	1.49	

† BASF(%) corresponds to the batch scale factor parameter obtained after the final refinement cycle, indicating the percentage of domain 2 in the structure.

diffraction experiments, enabling a better structural model to be obtained than in previous reports. A total of 109 428 reflections (3759 unique reflections) were collected at ambient conditions of pressure ( $1 \times 10^5 \text{ Pa}$ ) and temperature [ $T = 298$  (5) K] up to a resolution of  $0.69 \text{ \AA}^{-1}$  for crystal 1 (see the procedure mentioned above). The crystal structure determi-

nation resulted in final agreement factors  $R_1 = 0.0193$  and  $wR_2 = 0.0485$ . The largest residual peak obtained in the Fourier synthesis is  $0.73 \text{ e \AA}^{-3}$ , which is observed close to the iodine atom. In addition, we also performed a low-temperature data collection [ $T = 100$  (2) K] with the same crystal 1. The corresponding crystallographic data are shown in Table S5. Data

collection carried out with crystal 2 under ambient conditions (namely the crystal retrieved from the MDAC after the HPXRD experiments) showed a moderate quality after the compression–decompression cycle inside the MDAC (Table S2).

The authors of previous reports overlooked the fact that the lattice of their structure is strongly pseudo-orthorhombic (Dolenc & Modec, 2009). Indeed, an  $mP$  unit cell with a  $-a/2c \cos(\beta)$  ratio of 1 actually corresponds to an  $oB$  lattice. The unit-cell parameters of the  $P2_1/a$  unit cell have a ratio of  $-a/2c \cos(\beta) = 1.06$ , indicating a strong metric pseudo-symmetry of the lattice. To emphasize this metric pseudo-symmetry, we refined our data in the unconventional setting  $B2_1/e$  of the space group (Nespolo & Aroyo, 2016). Moreover, the unit cell of the unconventional setting  $B2_1/e$  of the space group also corresponds to the unit cell of the twinned sample at high pressure, in which the observed twin operation is a simple twofold rotation about the  $[100]$  axis. The transformation of the coordinate system from  $P2_1/a$  to  $B2_1/e$  is  $\mathbf{a}+2\mathbf{c}, \mathbf{b}, \mathbf{a}$  (from the  $P2_1/c$  setting, cell choice No. 1 of the space group, the transformation is  $2\mathbf{a}+\mathbf{c}, \mathbf{b}, \mathbf{c}$ ).

## 5. Structural rationale for twinning

Twinning can occur as the result of a phase transition (transformation twins), a physical action (mechanical twins) or a perturbation of the process of nucleation and growth (growth twins). Transformation twins typically result in domain structures, in which several physically distinct domains are distributed over a few (often two) orientations (domain states) (Nespolo, 2015). In mechanical twins, the interface between individuals is characteristically plane (Buerger, 1945) so that this type of twinning should result in contact twins. The twin we studied was obtained under pressure and could be either a transformation twin or a mechanical twin. However, no phase transition was observed in the range of pressure explored, ruling out the hypothesis of a transformation twin.

The relative orientation(s) of the individuals are mapped onto each other by isometries known as the twin operations. The reticular theory of twinning states that twin operations are crystallographic operations about a direct lattice element (Mallard's law; Friedel, 1926). These operations do not necessarily map the exact orientations of the individuals: a small deviation is often observed between the orientation obtained by applying the twin operation and the actual orientation of the domain. This deviation is measured (i) for reflection twins, by the angle between the lattice direction quasi-perpendicular to the twin plane and the irrational direction normal to it, or (ii) for rotation twins, by the angle between the lattice plane quasi-perpendicular to the twin axis and the irrational plane normal to it. This angle is known as the obliquity and indicated as  $\omega$ . When the twin operation is a rotation of order higher than two, imperfect lattice restoration may occur even for zero obliquity; in this case, a linear (as opposed to angular) parameter is used to measure the mismatch, known as the twin misfit (Nespolo & Ferraris, 2007). The Bravais lattice of NISac-py is almost exactly ortho-

rhombic, the  $\beta$  angle showing only a small deviation from  $90^\circ$  when the crystal structure is described in the unconventional setting  $B2_1/e$  of the space group. The twin lattice approximately coincides with the lattice of the individual (Figs. S3 and S4); twinning is therefore by pseudo-merohedry (twin index 1) and the obliquity  $\omega$  ranges from 1.5 to  $0.07^\circ$ , depending on the pressure (Tables 1 and 2). The twin operations are obtained by coset decomposition of the point group of the lattice, which is  $mmm$  when the obliquity is neglected, with respect to the point group of the structure, which is  $2/m$ .

$$mmm = \{1, 2_{[010]}, \bar{1}, m_{[010]}\} \cup \{2_{[100]}, 2_{[001]}, m_{[100]}, m_{[001]}\}. \quad (1)$$

The first coset is the point group of the structure, and the second coset is the twin law, which contains four twin operations. These would all be equivalent if the obliquity were zero; in our case, because of the small but non-zero obliquity, they correspond to slightly different orientations of the second individual, and the structure refinement showed that the actual twin operation is  $2_{[100]}$ . The twin point group is in this case straightforward, being the dichromatic extension of the point group of the crystal structure:  $2'/m'2/m'2'/m'$  (Nespolo, 2019).

A significant restoration of the lattice by the twin operation(s) is considered a necessary condition for twinning to occur. In order for two (or more) crystals to form an oriented association which is not just an accidental mechanical attachment (known as a bicrystal; Hahn *et al.*, 1999) a certain structural continuity across the interface is necessary. Because the lattice expresses the periodicity of the structure, without a significant lattice restoration such a structural continuity would be hardly possible. However, the lattice restoration is not sufficient to ensure a structural continuity. An empirical correlation between the degree of lattice restoration and the frequency of occurrence of twinning has been known since Friedel's times, but it does not explain why and how a twin forms.

An approach to studying the degree of structural continuity in twins was introduced by Marzouki *et al.* (2014a), based on an idea of Donnay & Curien (1960). Every crystal structure can be decomposed into finitely many crystallographic orbits. Each crystallographic orbit contains infinitely many atoms and is generated by applying the operations of the space group to an atom in the asymmetric unit. Each crystallographic orbit has an eigensymmetry that either coincides with the space group of the crystal structure (characteristic orbit) or with a supergroup of it (non-characteristic orbit). The eigensymmetry of the non-characteristic orbits may contain operations whose linear part coincides with the twin operation. If that is the case, then the crystallographic orbit may cross the interface between the two crystals without perturbation, or with only a small perturbation if the eigensymmetry is approximated (pseudo-eigensymmetry). This operation is called a *restoration operation*. If the number of crystallographic orbits possessing a restoration operation is significant, then the substructure that crosses the interface can be sufficiently important to explain the formation of the twin.

Table 3

Fractional atomic coordinates in the  $B2_1/e$  setting of the space group, optimized for pseudosymmetry with respect to  $Bmcb$ , origin in common.

$u_x$ ,  $u_y$ , and  $u_z$  are given in relative units.  $|u|$  is the absolute displacement given in Å. H atoms have been omitted because their positions were fixed and not refined.

Atom	$x$	$y$	$z$	$u_x$	$u_y$	$u_z$	$ u $
C1	0.4376	0.5370	0.1507	-0.0006	-0.0034	-0.0124	0.1507
C2	0.4870	0.5996	0.1498	0.0002	-0.0025	-0.0082	0.0989
C3	0.5133	0.6331	0.2500	0.0000	0.0000	-0.0085	0.1015
C4	0.4870	0.5997	0.3502	-0.0002	0.0025	-0.0082	0.0990
C5	0.4376	0.5370	0.3493	0.0006	0.0034	-0.0124	0.1505
C6	0.4117	0.5041	0.2500	0.0000	0.0000	-0.0105	0.1253
C7	0.3614	0.4408	0.2500	0.0000	0.0000	0.0115	0.1373
C8	0.1735	0.4092	0.6462	-0.0056	0.0662	-0.0791	1.0612
C9	0.1298	0.4594	0.6955	-0.0035	0.0355	-0.0579	0.7401
C10	0.1298	0.4593	0.8045	0.0035	-0.0355	-0.0579	0.7386
C11	0.1991	0.3358	0.7879	-0.0201	0.0073	-0.0131	0.5483
C12	0.2500	0.5000	0.6990	-0.0308	-0.1715	0.0000	1.4380
I1	0.2500	0.5000	0.4760	0.0267	-0.0949	0.0000	0.9591
N1	0.3514	0.4315	0.2500	0.0000	0.0000	0.1242	1.4826
N2	0.2500	0.5000	0.5921	-0.0369	-0.1029	0.0000	1.1979
O1	0.3888	0.7500	0.5000	0.0000	-0.0930	0.0167	0.6774
O2	0.4173	0.2500	0.5000	0.0000	0.0752	0.0119	0.5425
O3	0.3254	0.3931	0.2500	0.0000	0.0000	-0.0603	0.7198
S1	0.3973	0.2500	0.5000	0.0000	0.2416	-0.0496	1.7831

So far, several examples have been analysed by this approach, but they were all mineral crystals. We present here the first application to a molecular crystal. The structure of minerals is composed of coordination polyhedra polymerized in the three directions, and the restoration of some of the polyhedra across the interface is obtained if the corresponding atoms belong to a crystallographic orbit containing the restoration operation in its eigensymmetry. For a molecular crystal, not only do the atomic positions need to be restored, but also the chemical entity to which those atoms belong, otherwise the chemical continuity is not realized.

The first step of our investigation is to identify the minimal *translationengleiche* supergroups of  $B2_1/e$  corresponding to the arithmetic crystal class  $mmmB$  which are pseudo-symmetry groups of a substructure of our compound. There are six types of space group in this class (Nos. 63 to 68) and they all have  $B2_1/e$  among their maximal subgroups. However, only one,  $Bbem$  (No. 64, unconventional setting of  $Cmce$ ), has its coordinate system equally oriented with that of  $B2_1/e$  (*i.e.* the transformation matrix is the identity). All the others require a permutation of the basis vectors. There are however two possible origin shifts. Both  $B2_1/e$  and  $Bbem$  have two Wyckoff sets with site-symmetry group containing an inversion centre. The representatives of the two Wyckoff sets are, in both cases,  $(0, 0, 0)$  and  $(\frac{1}{4}, 0, \frac{1}{4})$ .  $Bbem$  can be obtained as an extension of  $B2_1/e$  either by keeping the origin in common or by moving it onto the other inversion centre, *i.e.* by an origin shift of  $(\frac{1}{4}, 0, \frac{1}{4})$ . For our structure, the second case, a non-zero shift of the origin, corresponds to a higher degree of structural pseudosymmetry, obtained by analysing the structure in the  $B2_1/e$  setting with the *PSEUDO* program (Capillas *et al.*, 2011) on the Bilbao Crystallographic Server (Aroyo *et al.*, 2006). The degree of pseudosymmetry is shown in Table 3, where the

atomic coordinates, idealized to be compatible with the  $Bbem$  symmetry, are listed. The fractional displacements  $u_x$ ,  $u_y$  and  $u_z$ , and the absolute displacements  $|u|$ , show the amount by which a representative of each crystallographic orbit has to be moved so that the space group of the crystal structure becomes  $Bbem$ . For several orbits the displacement is sufficiently small for the substructure built by those orbits to be considered pseudosymmetric in  $Bbem$ . This means that on applying the operations obtained by decomposing  $Bbem$  into cosets with respect to its maximal subgroup  $B2_1/e$ , the atoms in the substructure are mapped to positions close to those occupied by other atoms of the same chemical species of the substructure. Among those operations we find candidate restoration operations, *i.e.* operations which have the same linear part as the twin operation.

In order to understand better the meaning of the data in Table 3 let us consider an example. The crystallographic orbit C1 is obtained by applying all the infinitely many operations of  $B2_1/e$  to the atom C1 whose fractional coordinates are  $x = 0.4371$ ,  $y = 0.5336$ ,  $z = 0.1383$ . The restoration operation is an operation of  $Bbem$  which must have the same linear part as the twin operation, *i.e.* be a twofold rotation or screw rotation about  $[100]$ .  $Bbem$  has two such operations:  $2_x, \frac{1}{4}, \frac{1}{4}$  and  $2_1 x, \frac{1}{4}, 0$ . However, because of the shift of the origin by  $(\frac{1}{4}, 0, \frac{1}{4})$  from  $B2_1/e$  to  $Bbem$ , the possible restoration operations become  $2_x, \frac{1}{4}, 0$  and  $2_1 x, \frac{1}{4}, \frac{1}{4}$ . These would produce a pseudo-equivalent atom at  $x = 0.4371$ ,  $y = 0.9664$ ,  $z = 0.8617$  and at  $x = 0.9371$ ,  $y = 0.4664$ ,  $z = 0.3617$ , respectively. The second result is close to the position of C5, *i.e.*  $x = 0.4382$ ,  $y = 0.9596$ ,  $z = 0.8369$ . If C1 is moved by  $0.1507$  Å onto the position  $x = 0.4376$ ,  $y = 0.5370$ ,  $z = 0.1507$  and C5 is moved by  $0.1507$  Å onto the position  $x = 0.4376$ ,  $y = 0.9630$ ,  $z = 0.8493$ , then the two atoms would be exactly mapped by the operation  $2_x, \frac{1}{4}, 0$ . The same holds for the other atoms. The restoration operation is therefore  $2_x, \frac{1}{4}, 0$ .

Table 3 shows that atoms C1 to C7 are restored within less than  $0.2$  Å, six more atoms (C9 to C11 and the O atoms) are restored within less than  $1$  Å and the other atoms should move more than  $1$  Å to fit the supergroup symmetry.

The amount (number of crystallographic orbits) and degree (displacement needed to fit the supergroup symmetry) are not the only factors to consider. For a twin to form and be stable, a significant structural continuity is required at the interface, not away from it. This means that the quasi-restoration of crystallographic orbits is a necessary condition not everywhere in the structure but in the proximity of the composition surface. Fig. 3 shows the structure in the two orientations, overlapped. Atoms in black and white correspond to a degree of restoration that requires a displacement  $|u| < 1$  Å, and those in red and yellow are atoms for which  $|u| > 1$  Å. Clearly, the pseudo-restoration is realized around the boundary of the unit cell, whereas a larger divergence occurs away from it, *i.e.* in a region where the presence of the second domain does not exert a significant influence. The location of the composition surface that corresponds to the best restoration is therefore at  $x = 0$ ; because the unit cell is *B*-centred, the same degree of restoration is realized at  $x = \frac{1}{2}$  as well. The structure of the twin

can therefore be described by taking one orientation on one side of the composition surface located at  $x = 0$  or  $x = \frac{1}{2}$ , and the other orientation on the opposite side, as shown in Fig. 4, drawn assuming the composition surface at  $x = 0$ . The sulfonyl groups, which are in a *trans* orientation in the untwinned crystal, are *cis*-oriented in the twinned structure, but they are sufficiently far away from the composition plane for this difference to be ineffective in preventing the formation of the twin. The figure corresponds to freezing the formation of the twin at the first step. The importance of these relaxations, in particular from the energetic viewpoint, is discussed in the next section.

## 6. Discussion

### 6.1. Equation of state

The variation in the unit-cell volume as a function of pressure was plotted for the experimental data points and fitted with a third-order Birch–Murnaghan equation of state (EOS) (Angel, 2000) using the *EosFit7-GUI* software (Gonzalez-Platas *et al.*, 2016). The unit-cell volume changes monotonically as a function of pressure without any peculiar characteristic and/or discontinuity, reducing overall by 19.8% between the lowest and highest measured pressures [Fig. 5(a)]. This is observed with both increasing (blue circle data) and decreasing (red circle data) pressures, leading to a unique and consistent data set that can be fitted with the same EOS, whereas fitting these two subsets of data separately leads to equivalent fitting parameters with larger standard deviations (Fig. S5). After fitting, the determined EOS parameters are: reference volume  $V_0 = 2705$  (11) Å<sup>3</sup>, bulk modulus  $K_{T_0} = 7$  (1) GPa and the first derivative of the bulk modulus  $K'_{T_0} =$

11 (3). A small bulk modulus (typically <10 GPa) is characteristic of a soft material (like our organic crystal), where the intermolecular interactions are mainly dominated by dispersion forces and/or electrostatic interactions. The fitted value of the bulk modulus is also consistent with those previously reported for other soft materials in the literature (Likhacheva *et al.*, 2014; Slebodnick *et al.*, 2004). On the other hand, considering the uncertainties associated with the experimental values of pressure, all data lie on the EOS curve (black dotted lines). This trend indicates that no hysteresis is associated with the compression–decompression cycle. In other words, the shrinking of the unit-cell volume during the compression process shows a reversible recovery on its expansion via the decompression process. Thus, the experimental data were treated as a single data set rather than two separate data subsets.

In order to validate the experimental findings, the EOS is also represented for the calculated theoretical data, where the corresponding reduction in the unit-cell volume was found to be 20.6% between the lowest and highest calculated pressures. Further fitting using the same third-order Birch–Murnaghan EOS yields  $V_0 = 2689$  (9) Å<sup>3</sup>,  $K_{T_0} = 6.8$  (5) GPa and  $K'_{T_0} = 10.8$  (8), showing quite good agreement with the values obtained experimentally. Fig. 5(b) shows that both the experimental (blue dotted lines) and theoretical (red dotted lines) EOS curves are in good agreement with each other. The small offset observed between them might be associated with the temperature effect, considering that all the theoretical data were calculated omitting this thermodynamic parameter. In order to compensate for this effect, corrections were made to the values of pressures assigned to the theoretical data set, based on the hypothesis that a volume similar to the one observed under ambient conditions should correspond to the theoretically calculated one with pressure equal to 0 GPa.

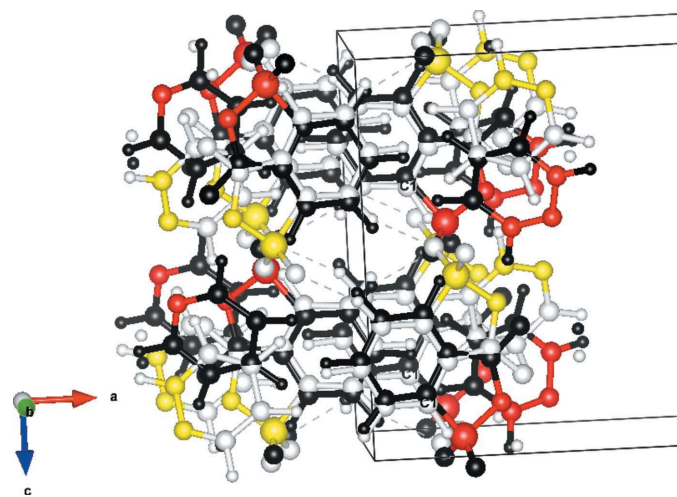


**Figure 3**  
The structure of NISac-py twinned by a twofold rotation around the [100] direction in the  $B2_1/e$  setting of the space group. The two substructures quasi-overlapped by the restoration operation are shown in white and black, respectively. The mismatch is shown in yellow and red. This mismatch occurs sufficiently far away from the composition surface to represent a minor obstacle to the formation of the twin. Figure drawn with *VESTA* (Momma & Izumi, 2011).

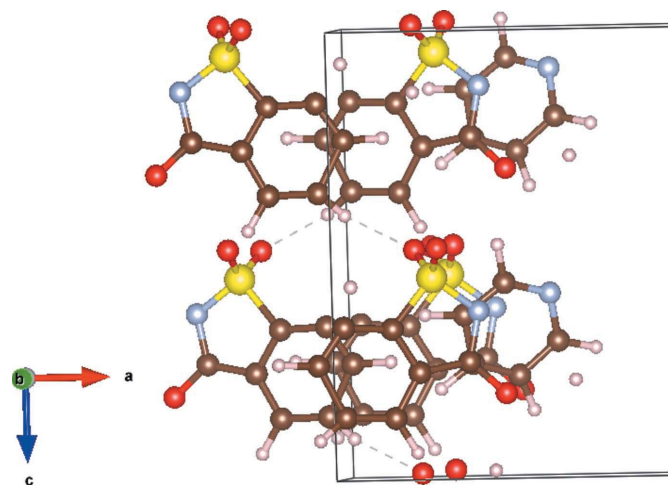


**Figure 4**  
Part of the twinned structure of NISac-py close to the composition plane. The figure is obtained by taking one orientation on one side of the composition surface and the other orientation on the opposite side. The connectivity across the composition surface is maintained, although the C–C distances are stretched to unphysical values. The figure therefore corresponds to freezing the formation of the twin at the first step. Figure drawn with *VESTA* (Momma & Izumi, 2011).

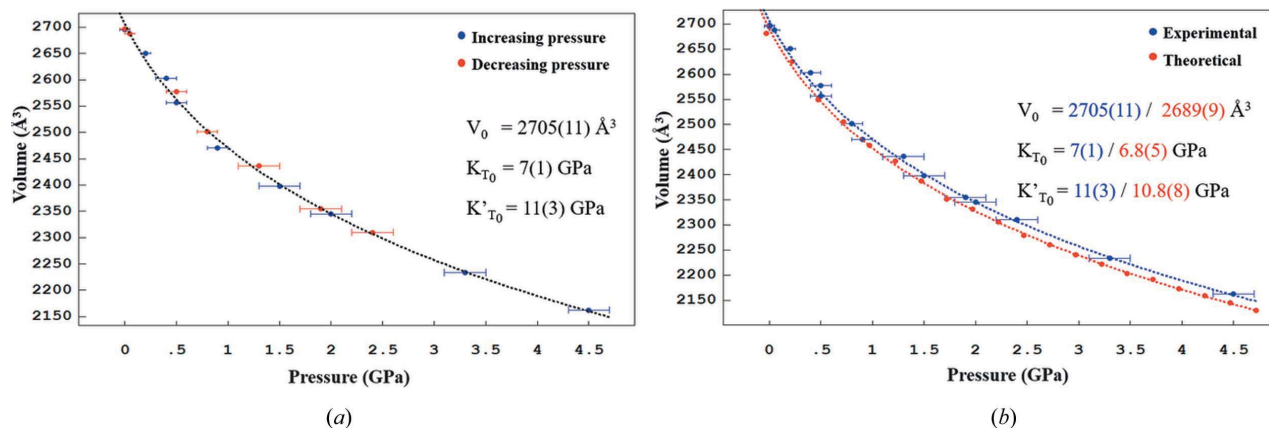


**Figure 5**  
 (a) The variation in the unit-cell volume as a function of pressure fitted with a third-order Birch–Murnaghan EOS using experimental data. Blue circles denote increasing pressure data, red circles denote decreasing pressure data and the black dotted line is the EOS fitting curve. (b) Experimental and theoretical EOS curves plotted together. Blue circles denote experimental data, the blue dotted line is the experimental EOS fitting curve, red circles denote theoretical data and the red dotted line is the theoretical EOS fitting curve. The values of EOS parameters obtained after the refinement process are given with the corresponding plots. Standard uncertainties associated with the volume of the unit cell are too small to be visible in the plots.

### 6.2. Variation in unit-cell parameters with pressure

A plot of the relative changes in the unit-cell parameters as a function of pressure shows different compressibilities along different crystallographic directions. This feature may be linked to the anisotropic strain generated on the application of hydrostatic pressure, resulting from the anisotropic nature of intermolecular interactions taking place in the crystal packing (see Section 6.5). Fig. 6(a) shows, for experimental data, the variation in the unit-cell parameters with pressure [relative to the values  $a_0$ ,  $b_0$  and  $c_0$  obtained at 0.00 (5) GPa, the starting

pressure taken as the reference], indicating that the compressibility along the  $b$  direction is more pronounced than along the  $c$  and  $a$  directions. In the explored range of pressures, the compressibility along the direction of each unit-cell axis is calculated as the ratio  $\Delta l/l_0$  ( $l = a, b$  or  $c$ ), where  $\Delta l = l_{0.00(5)\text{ GPa}} - l_{4.5(2)\text{ GPa}}$ . The maximum compressibility of 11% is observed along the  $b$  direction, followed by 5.5% along the  $c$  direction. The crystal structure is more rigid along the  $a$  direction, with a compressibility of only 4.7% between the lowest and highest achieved pressures. A similar trend is

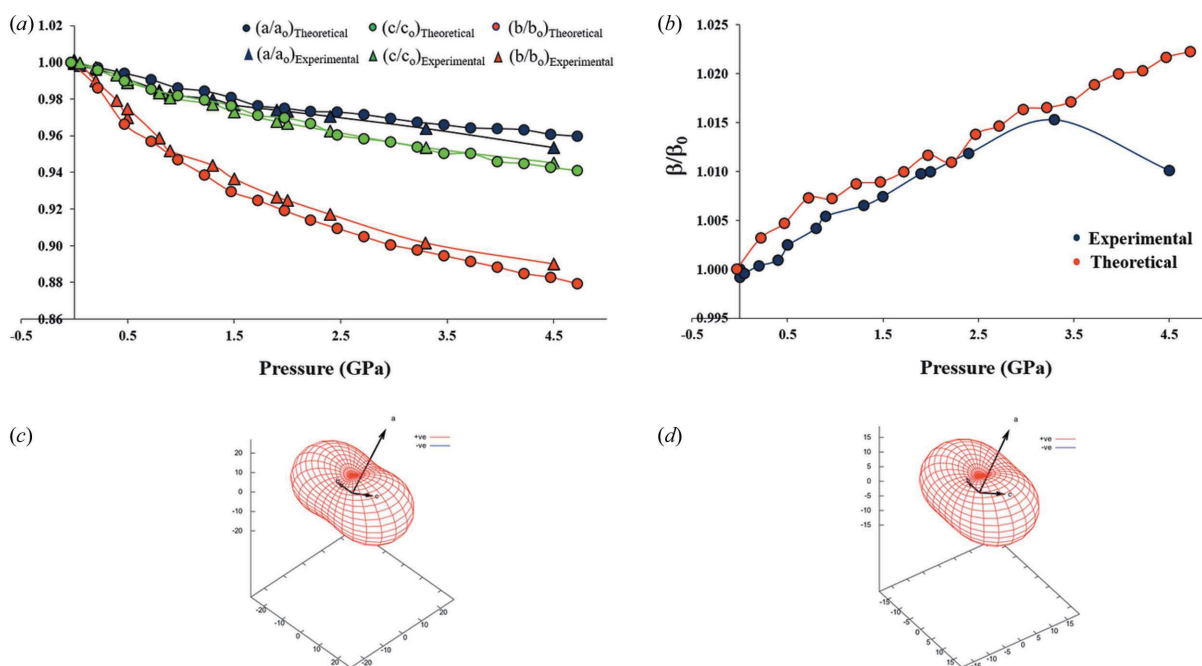


**Figure 6**  
 Plots of the variation with pressure of (a) the unit-cell parameters and (b) the unit cell  $\beta$  angle relative to the values observed at the starting pressure [0.00 (5) GPa] for experimental and theoretical data. The compressibility indicatrix is depicted for (c) experimental and (d) theoretical data. Positive compressibilities (red surfaces) are observed in all directions. Curves connecting the data are plotted to guide the eye.

observed with the theoretical data [Fig. 6(a)], where the maximum compressibility also shows along the *b* direction. Furthermore, the theoretical compressibility values are in good agreement with the experimental ones: 12.1% for the *b* direction, followed by 5.9% and 4% for the *c* and *a* directions, respectively. The monoclinic angle relative to the value measured at the starting pressure [0.00 (5) GPa] increases as a function of pressure in both experimental and theoretical data sets [Fig. 6(b)].

The principal axes of compression and the corresponding compressibilities were calculated for the experimental and theoretical data sets using the *PASCal* web tool (Principal Axis Strain Calculator, <http://pascal.chem.ox.ac.uk>) (Table S6). The first principal axis of compression (denoted  $X_1$ ) is along the crystallographic *b* direction for both experimental and theoretical data sets, while the corresponding compressibility values (denoted  $K_1$ ) are calculated for the same data sets as 27 (2) and 18.9 (8) TPa<sup>-1</sup>, respectively. The second and third principal axes of compression are oriented in the *ac* plane. Figs. 6(c) and 6(d) show the compressibility indicatrix, a three-dimensional representation of the principal compressibilities oriented with respect to the crystallographic axes landmark, for experimental and theoretical data.

### 6.3. Mechanical twinning

As discussed above, mechanical twinning is observed along the high-pressure structures, the twinned sample presenting two domains. The larger and smaller domains are hereafter called domain 1 and domain 2, respectively. The two domains are mapped by a twofold rotation along the [100] direction of the unit cell. Fig. 7 shows the percentage variation in the domain 2 volume as a function of pressure. This percentage is obtained from the value of the BASF (batch scale factor) parameter, which is estimated after the final refinement of the high-pressure structures. Domain 2 is not detected (~0%) at 0.00 (5) GPa and gradually increases with pressure, reaching a value of 14.48 (13)% at 4.5 (2) GPa. The pressure-transmitting medium used in this study (Daphne oil 7474) is known to solidify at 3.7 GPa at room temperature (Murata *et al.*, 2008), a feature that may cause a loss of hydrostatic conditions inside

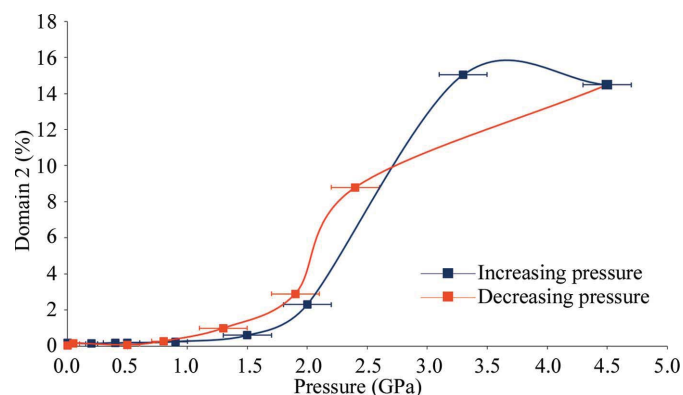


**Figure 7**  
The percentage variation in domain 2 plotted as a function of pressure. Curves connecting the data are plotted to guide the eye.

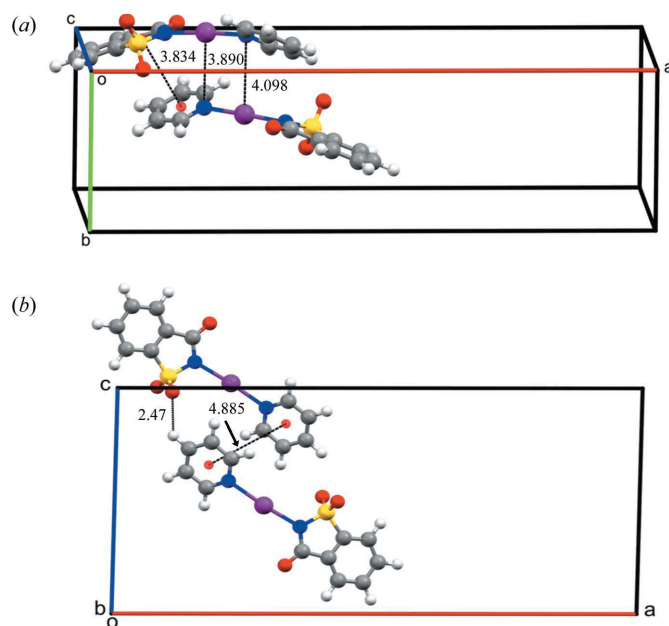
the sample chamber. In this respect, it has been observed experimentally that the percentage of domain 2 increases monotonically with compression up to 3.3 (2) GPa. Increasing the pressure further, beyond the value at which the transmitting medium is expected to solidify, the percentage of domain 2 decreases slightly [15.02 (9)% at 3.3 (2) GPa and 14.48 (13)% at 4.5 (2) GPa]. On releasing the pressure, domain 2 reduces to 8.8 (2)% at 2.4 (2) GPa, which corresponds to the highest pressure measured in the decompression process. Finally, it disappears (~0%) after the complete removal of the applied pressure. Hence, after a complete cycle of compression–decompression, it can be concluded that the mechanical twinning is reversible and that the percentage of domain 2 is dependant on the applied pressure.

### 6.4. Crystal structure description under ambient conditions

In the NISac-py adduct the I atom lies in between the N atoms of *N*-iodosaccharin and pyridine [Fig. 1(a)], slightly closer to the former [N1–I1 = 2.2305 (16) Å] than to the latter [I1–N2 = 2.2875 (16) Å]. Accordingly, the adduct is assembled by means of a halogen-bonding interaction involving the electropositive  $\sigma$ -hole region of the I atom belonging to *N*-iodosaccharin as the halogen-bonding donor [ $V_{S,max}$  = 283.3 kJ mol<sup>-1</sup>; Fig. S6(b)] and the electronegative N atom of pyridine [ $V_{S,min}$  = -181.6 kJ mol<sup>-1</sup>; Fig. S6(c)] as the halogen-bonding acceptor.

### 6.5. Energetic and electronic analyses of intermolecular interactions under ambient conditions

Energetic analysis of the intermolecular interactions, performed with *CrystalExplorer* on the crystal structure under ambient conditions, reveals that the crystal packing is governed by two main interactions (Table S7). The first one (total interaction energy of -80.9 kJ mol<sup>-1</sup>) corresponds to the stacking of the adducts along [010], involving  $\pi$ - $\pi$  interactions between the pyridine and *N*-iodosaccharin rings [Fig. 8(a)], as well as a favourable electrostatic interaction between the positively charged halogen atom I1 [ $Q(I) = 0.48 e$ ] and the negatively charged pyridine N atom [ $Q(N_{py}) = -1.20 e$ ] of neighbouring adducts [N2...I1( $\frac{1}{2} - x, \frac{1}{2} + y, 1 - z$ ) = 3.890 Å and I1...N2( $\frac{1}{2} - x, -\frac{1}{2} + y, 1 - z$ ) = 4.098 Å]. Following the energetic ranking, the next dimer of adducts that shows a significant interaction energy corresponds to that formed around an inversion centre (-79.4 kJ mol<sup>-1</sup>), involving a couple of symmetry-related hydrogen bonds C10–H10...O1( $\frac{1}{2} - x, 1 - y, \frac{3}{2} - z$ ) ( $d_{H...O} = 2.47$  Å,  $\alpha_{C-H...O} = 131^\circ$ ). Although of similar interaction energy, the energy decomposition shows that this second interaction is formed differently from the first one. Indeed, even showing a similar electrostatic contribution, they differ in dispersion and repulsion contributions, whose variations almost compensate each other. This is in line with the fact that the aromatic rings are here observed at a longer distance than in the previous dimer interaction [inter-centroid py...py( $\frac{1}{2} - x, 1 - y, \frac{3}{2} - z$ ) = 4.885 Å] [Fig. 8(b)].


**Figure 8**

Dimers extracted from the experimental crystal structure under ambient conditions. (a) The strongest interaction of NISac-py with its environment involving a  $\pi$ - $\pi$  stacking interaction between the symmetry-related  $(x, y, z)$  and  $(\frac{1}{2} - x, -\frac{1}{2} + y, 1 - z)$  adducts. (b) The interaction between the symmetry-related  $(x, y, z)$  and  $(\frac{1}{2} - x, 1 - y, \frac{3}{2} - z)$  NISac-py adducts. Characteristic distances (in Å) of relevant interactions (shown as dashed lines) are given.

These two main contacts form (200) NISac-py adduct planes in the  $B2_1/e$  setting, whose cohesion is reinforced by three additional interactions of the  $(x, y, z)$  reference molecule with neighbours. The first one involves the symmetry-related adduct  $(\frac{1}{2} - x, 1 - y, \frac{1}{2} - z)$ , forming a dimer around an inversion centre and being characterized by the hydrogen bond  $C8-H8 \cdots O3(\frac{1}{2} - x, 1 - y, \frac{1}{2} - z)$  ( $d_{H \cdots O} = 2.52$  Å,  $\alpha_{C-H \cdots O} = 173^\circ$ ) and a relatively close favourable electrostatic interaction between an I atom and a carbonyl O atom,  $C7-O3 \cdots I1(\frac{1}{2} - x, 1 - y, \frac{1}{2} - z)$  [ $d_{O \cdots I} = 4.244$  Å,  $\alpha_{C-O \cdots I} = 148^\circ$ ,  $Q(I1) = 0.48$  e,  $Q(O3) = -1.17$  e] (Fig. S7). The second interaction involves the symmetry-related molecule  $(x, \frac{1}{2} - y, -\frac{1}{2} + z)$  through a unique hydrogen bond  $C12-H12 \cdots O3$  ( $d_{H \cdots O} = 2.41$  Å,  $\alpha_{C-H \cdots O} = 165^\circ$ ) (Fig. S8). Finally, the third one involves the symmetry-related molecule  $(x, \frac{3}{2} - y, -\frac{1}{2} + z)$ , which is barely stabilizing and is characterized by the proximity between atom O1 of the sulfonyl group of the neighbouring NISac entity and atom C1 of the  $\pi$  plane of the NISac molecule that is slightly electropositive in the adduct (Fig. S9) [ $d_{C1 \cdots O1} = 3.328$  Å,  $Q(O1) = -1.36$  e,  $Q(C1) = 0.02$  e].

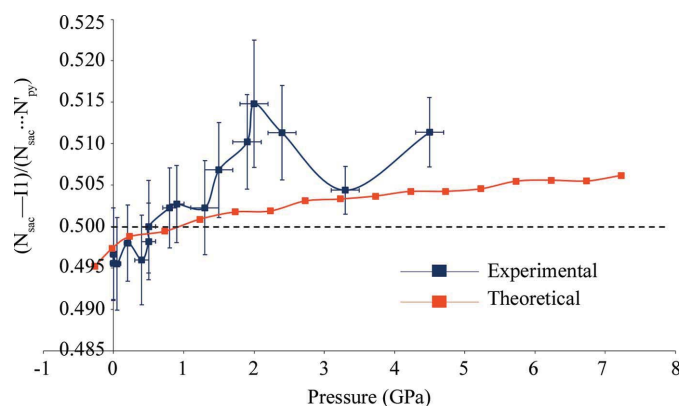
Adjacent (200) adduct planes (Fig. S10) interact through two main interactions of moderate intensity ( $E_{\text{int}} = -27.2$  and  $-22.3$  kJ mol $^{-1}$ ). The first one, which has a significant electrostatic component (Table S7), corresponds to the formation of a cyclic hydrogen bond between two NISac entities through the sulfonyl O atom and an H atom of the aryl ring,  $C4-H4 \cdots O2(1 - x, 1 - y, 1 - z)$  ( $d_{H \cdots O} = 2.35$  Å,  $\alpha_{C-H \cdots O} = 160^\circ$ ) (Fig. S11), whereas the second one involves a

long  $C2-H2 \cdots O2$  contact ( $d_{H \cdots O} = 2.79$  Å,  $\alpha_{C-H \cdots O} = 130^\circ$ ) with a stabilization that is mainly driven by the dispersion contribution due to the proximity of the aromatic rings (Fig. S12). Two additional minor interactions ( $E_{\text{int}} \simeq -5$  kJ mol $^{-1}$ ) with main dispersion contribution correspond to the proximity of aromatic rings (Figs. S13 and S14).

### 6.6. Variation in intermolecular interactions with pressure

It has been observed from the EOS analysis that, on compression, the unit-cell volume reduces by  $\sim 20\%$  for both experimental and theoretical data. This induces a variation in the relative positions of the molecular complexes in space, in most cases approaching towards each other. However, for some of them, either they do not change their relative distances significantly (due to the less compressible behaviour of specific intermolecular interactions) or they separate slightly from each other because some interactions can not be compressed as much as others when applying pressure.

One of the most important intermolecular interactions that form the NISac-py crystal structure is the  $N_{\text{sac}} \cdots I \cdots N'_{\text{py}}$  halogen-bonding motif (termed  $N1 \cdots I1 \cdots N2$  based on the atom-numbering scheme). The structural modification of this halogen-bonding motif has been investigated as a function of external pressure, both experimentally and theoretically. It has been observed that, on hydrostatic compression, the  $N_{\text{sac}} \cdots N'_{\text{py}}$  distance decreases gradually along with the variation in the  $N_{\text{sac}} \cdots I$  and  $I \cdots N'_{\text{py}}$  distances (Table S8). Thus, in order to determine the relative shift of the I atom from the donor to the acceptor in the halogen-bonding motif, we have followed the evolving behaviour of the  $N_{\text{sac}} \cdots I$  and  $I \cdots N'_{\text{py}}$  distances normalized to that of  $N_{\text{sac}} \cdots N'_{\text{py}}$ . Fig. 9 shows the variation in the normalized distance  $(N_{\text{sac}} \cdots I)/(N_{\text{sac}} \cdots N'_{\text{py}})$  as a function of pressure for both experimental and theoretical data. The horizontal black dotted line indicates the middle position (normalized distance of 0.5) between  $N_{\text{sac}} \cdots N'_{\text{py}}$ , guiding whether I1 is closer to the donor N atom ( $N_{\text{sac}}$ ) or the acceptor N atom ( $N'_{\text{py}}$ ) at each pressure. The I atom shifts slightly closer to  $N'_{\text{py}}$  above 1 GPa, but is very close to the middle position between donor and acceptor. This


**Figure 9**

The variation in the normalized bonding distance  $(N_{\text{sac}} \cdots I)/(N_{\text{sac}} \cdots N'_{\text{py}})$  as a function of pressure. Curves connecting the data are plotted to guide the eye. Error bars are shown for experimental data.

feature does not permit us to conclude anything about the transfer of the I atom from the donor to the acceptor, but rather points to an intermediate situation where both donor and acceptor exert a similar interaction strength on the I atom. In addition to the fact that the donor and acceptor entities are electronically different (and therefore the middle position can not be considered as the exact transition geometry in the transfer), the large uncertainties associated with these structural distances hinder any conclusion about the precise position of atom I1 within the adduct. These large uncertainties are mainly associated with the poor completeness of the HPXRD data, which is close to 40% up to a resolution of  $0.56 \text{ \AA}^{-1}$  in all cases (mainly due to the experimental constraints).

Once the full cycle of compression–decompression is reached (decompression finishes with the complete removal of pressure, coming back to ambient pressure), the unit-cell parameters and volume regain their initial values, and the NISac-py complex (including iodine) is back to its initial geometry. The same trends were observed with the theoretical data (Table S9), where the transition above the middle point between  $N_{\text{sac}}$  and  $N'_{\text{py}}$  is found to be in the same range of pressures, validating the experimental findings. On the other hand, as the  $N_{\text{sac}} \cdots \text{I} \cdots N'_{\text{py}}$  angle is close to  $180^\circ$  at any investigated pressure, the normalized distance  $(\text{I} \cdots N'_{\text{py}}) / (N_{\text{sac}} \cdots N'_{\text{py}})$  evolves in the opposite way to  $(N_{\text{sac}} \cdots \text{I}) / (N_{\text{sac}} \cdots N'_{\text{py}})$  as a function of pressure (Fig. S15). Within the investigated range of pressures, the  $N_{\text{sac}} - \text{I} \cdots N'_{\text{py}}$  angle shows maximum variations of only  $2.70^\circ$  and  $2.34^\circ$  for the experimental and theoretical data, respectively [Tables S8 and S9, and Fig. S16(a)], while the angle between the molecular planes formed by the saccharin ring (excluding I and H atoms) and the pyridine ring (excluding H atoms) remains mainly unchanged (only very small variations of  $1.17^\circ$  and  $2.32^\circ$  are observed for the experimental and theoretical data, respectively) [Tables S8 and S9, and Fig. S16(b)].

In order to investigate the effect of the crystalline environment on the migration of the I atom, selected non-covalent interactions around I1 were studied as a function of pressure. For the structure determined under ambient conditions, four of the nine independent crystallographic dimers (Section 6.5) exhibit an intermolecular interaction involving I1 [namely, those formed by a central complex  $(x, y, z)$  and another generated by either of the symmetry operations (i)  $(\frac{1}{2} - x, -\frac{1}{2} + y, 1 - z)$ , (ii)  $(\frac{1}{2} - x, 1 - y, \frac{3}{2} - z)$ , (iii)  $(x, \frac{1}{2} - y, \frac{1}{2} + z)$  or (iv)  $(\frac{1}{2} - x, \frac{1}{2} + y, 1 - z)$ ]. The experimental distances of the intermolecular interactions involving iodine in the above-mentioned dimers decrease monotonically with increasing hydrostatic pressure, whereas the observed hydrogen-bonding angles with iodine show a non-monotonic behaviour and do not deviate significantly from their initial values (Table S10, and Figs. S17 and S18). The theoretical distances are in quite good agreement with the experimental ones, following very similar trends (Table S11, and Figs. S17 and S18). Considering the experimental values of the reduction ratio (RR), out of the ten contacts the  $\text{I1}(x, y, z) \cdots \text{C8}(\frac{1}{2} - x, -\frac{1}{2} + y, 1 - z)$  interaction seems the

most significant at 4.5 (2) GPa [ $\text{RR}_{4.5(2)\text{GPa}} = 0.91$ ], followed by  $\text{I1}(x, y, z) \cdots \text{I1}(\frac{1}{2} - x, -\frac{1}{2} + y, 1 - z)$  [ $\text{RR}_{4.5(2)\text{GPa}} = 0.96$ ] and  $\text{I1}(x, y, z) \cdots \text{H8}(\frac{1}{2} - x, -\frac{1}{2} + y, 1 - z)$  [ $\text{RR}_{4.5(2)\text{GPa}} = 0.96$ ]. On the other hand, the maximum variation in RR is observed for the  $\text{I1}(x, y, z) \cdots \text{I1}(\frac{1}{2} - x, -\frac{1}{2} + y, 1 - z)$  interaction [ $\Delta(\text{RR}) = 0.14$ ]. Similar behaviour is observed with the theoretical data, where maximum changes occur for the  $\text{I1}(x, y, z) \cdots \text{O3}(x, \frac{1}{2} - y, \frac{1}{2} + z)$  [ $\Delta(\text{RR}) = 0.15$ ] and  $\text{I1}(x, y, z) \cdots \text{I1}(\frac{1}{2} - x, -\frac{1}{2} + y, 1 - z)$  [ $\Delta(\text{RR}) = 0.14$ ] interactions. Accordingly, upon the action of external pressure, the crystalline environment around the I atom undergoes a significant modification that is transmitted to the interactions with the latter, therefore favouring the migration of the I atom between atoms  $N_{\text{sac}}$  (N1) and  $N'_{\text{py}}$  (N2).

### 6.7. Energetic analysis of mechanical twinning

The above results show that the structure consists of strongly cohesive (200) planes bonded through weaker interactions. As the twin operation is a simple twofold rotation quasi-perpendicular to these planes, we performed periodic DFT calculations in order to quantify the energetic cost of the twinning at the composition plane. Taking the experimental structure obtained at 3.3 (2) GPa (which is the one with the best structural model), the H atoms were first placed at normalized neutron distances. Since we were interested in the composition plane, we then considered only the NISac and py molecules that are the closest to  $x = 0$  and  $x = 1$ , defining sub-slabs *A* and *B*, respectively (*i.e.* the molecules close to  $x = \frac{1}{2}$  are not considered here). Two structural models were then built (Fig. S19): the first one corresponds to the untwinned structure (sub-slabs *A* and *B* are from the original structure model), whereas in the second one the sub-slab *B* is modified by the twin twofold rotation operation along [100], thus creating, due to the periodic boundary conditions of the calculation, the twin composition plane *A/B*. Single-point calculations were performed using identical conditions on these two models, and also on models considering only sub-slab *A* or *B* separately. The  $x = 0$  interface in both cases (untwinned and twinned) is observed to be stabilizing, the *AB* system being lower in energy than that resulting from the addition of those corresponding to the isolated *A* and *B* systems. Remarkably, the stabilizing energy difference between the untwinned and twinned interfaces is only  $6.4 \text{ kJ mol}^{-1}$  in favour of the former structure. In other words, since the interface consists of four NISac-py adducts, the twinning of this structure costs only  $1.6 \text{ kJ mol}^{-1}$  per NISac-py adduct.

## 7. Conclusions

The NISac-py adduct shows a crystal structure that is able to follow a reversible modification upon a cycle of compression–decompression induced by external pressure, as shown by the evolving behaviour of the unit-cell parameters and volume. Consequently, the reversibility is also exhibited in the observed twin volume. This feature can be explained by the very low energetic cost involved in the twinning process.

The reversibility of the crystal structure implies reversibility in the position of iodine within the adduct, which in addition to the main donor and acceptor electronic influences is also partially driven by secondary interactions with the molecular environment. As in this family of crystals the position of iodine within the adduct is associated with the charge on the donor and acceptor entities, and therefore with the co-crystal versus salt nature of the crystal structure, one can expect to drive the electronic properties of the solid in a switch on/switch off manner upon increasing/decreasing pressure (or with any other external stimulus), controlling the reversible modification of the environment. While the I atom is closer to the donor under ambient conditions, it is positioned close to the middle position between the donor and acceptor entities along the range of investigated pressures, as indicated by the normalized  $(N_{\text{sac}} \cdots I)/(N_{\text{sac}} \cdots N'_{\text{py}})$  and  $(I \cdots N'_{\text{py}})/(N_{\text{sac}} \cdots N'_{\text{py}})$  values that are very close to 0.5. Accordingly, even if both experimental and theoretical data seem to indicate a monotonic shift of iodine from the donor to the acceptor with increasing pressure, the system cannot be considered as a salt (with a fully transferred iodine) but rather as a co-crystal in a frozen transferral process, where the donor and acceptor entities have to be considered in an intermediate situation between their neutral and ionic forms. Further, the nature of  $N_{\text{donor}} \cdots I$  and  $I \cdots N_{\text{acceptor}}$  bonding interactions cannot be determined from structural data only. An electron-density analysis is required to resolve the issue, as described by Makhotkina *et al.* (2015) and Aubert *et al.* (2017), where the co-crystal versus salt situation was studied for a family of similar complexes involving *N*-iodosuccinimide, *N*-iodosaccharin and *N*-bromosaccharin as donors, and pyridine, 4-picoline and 4-dimethylaminopyridine as acceptors. In this regard, additional work is currently under development for the current family of systems under pressure.

## 8. Related literature

For further literature related to the supporting information, see Dolenc (2000) and Voute *et al.* (2016).

## Acknowledgements

We thank the EXPLOR mesocentre for computing facilities (Project 2019CPMXX0984) and the PMD<sup>2</sup>X X-ray diffraction facility of the Institut Jean Barriol (Université de Lorraine) for X-ray diffraction measurements (<http://crm2.univ-lorraine.fr/lab/fr/services/pmd2x>).

## Funding information

VVS thanks the French National Agency for Research (ANR project 17-CE07-0025-01) and the Region Grand-Est (project 18P07531-18\_GE4\_156 No. AAP-011-011 SIGMAHOLE) for financial support. This work has been supported by ANR (France) under contract Nos. ANR-17-CE07-0025-01 (Nancy) and ANR-17-CE07-0025-02 (Rennes).

## References

- Angel, R. J. (2000). *Rev. Mineral. Geochem.* **39**, 85–104.
- Aroyo, M. I., Perez-Mato, J. M., Capillas, C., Kroumova, E., Ivantchev, S., Madariaga, G., Kirov, A. & Wondratschek, H. (2006). *Z. Kristallogr.* **221**, 15–27.
- Aubert, E., Espinosa, E., Nicolas, I., Jeannin, O. & Fourmigué, M. (2017). *Faraday Discuss.* **203**, 389–406.
- Boldyreva, E. V., Kolesnik, E. N., Drebushchak, T. N., Ahsbahs, H., Beukes, J. A. & Weber, H.-P. (2005). *Z. Kristallogr.* **220**, 58–65.
- Brog, J.-P., Chanez, C.-L., Crochet, A. & Fromm, K. M. (2013). *RSC Adv.* **3**, 16905.
- Bruker (2019). APEX3. Version 2019.11. Bruker AXS Inc., Madison, Wisconsin, USA.
- Buerger, M. J. (1945). *Am. Mineral.* **30**, 469–482.
- Capillas, C., Tasci, E. S., de la Flor, G., Orobengoa, D., Perez-Mato, J. M. & Aroyo, M. I. (2011). *Z. Kristallogr.* **226**, 186–196.
- Cavallo, G., Metrangolo, P., Milani, R., Pilati, T., Priimagi, A., Resnati, G. & Terraneo, G. (2016). *Chem. Rev.* **116**, 2478–2601.
- Clark, S. J., Segall, M. D., Pickard, C. J., Hasnip, P. J., Probert, M. J., Refson, K. & Payne, M. C. (2005). *Z. Kristallogr.* **220**, 567–570.
- Dawson, A., Allan, D. R., Parsons, S. & Ruf, M. (2004). *J. Appl. Cryst.* **37**, 410–416.
- Desiraju, G. R., Ho, P. S., Kloo, L., Legon, A. C., Marquardt, R., Metrangolo, P., Politzer, P., Resnati, G. & Rissanen, K. (2013). *Pure Appl. Chem.* **85**, 1711–1713.
- Dolenc, D. (2000). *Synlett*, **2000**, 544–546.
- Dolenc, D. & Modec, B. (2009). *New J. Chem.* **33**, 2344–2349.
- Dolomanov, O. V., Bourhis, L. J., Gildea, R. J., Howard, J. A. K. & Puschmann, H. (2009). *J. Appl. Cryst.* **42**, 339–341.
- Donnay, J. D. H. & Curien, H. (1960). *Cursillos y Conferencias del Instituto 'Lucas Mallada'*, Vol. 7, pp. 13–14. Barcelona: CSIC.
- Friedel, G. (1926). *Leçons de Cristallographie*. Nancy: Berger-Levrault.
- Frisch, M. J., Trucks, G. W., Schlegel, H. B., Scuseria, G. E., Robb, M. A., Cheeseman, J. R., Scalmani, G., Barone, V., Mennucci, B., Petersson, G. A., Nakatsuji, H., Caricato, M., Li, X., Hratchian, H. P., Izmaylov, A. F., Bloino, J., Zheng, G., Sonnenberg, J. L., Hada, M., Ehara, M., Toyota, K., Fukuda, R., Hasegawa, J., Ishida, M., Nakajima, T., Honda, Y., Kitao, O., Nakai, H., Vreven, T., Montgomery, J. A. Jr, Peralta, J. E., Ogliaro, F., Bearpark, M., Heyd, J. J., Brothers, E., Kudin, K. N., Staroverov, V. N., Keith, T., Kobayashi, R., Normand, J., Raghavachari, K., Rendell, A., Burant, J. C., Iyengar, S. S., Tomasi, J., Cossi, M., Rega, N., Millam, J. M., Klene, M., Knox, J. E., Cross, J. B., Bakken, V., Adamo, C., Jaramillo, J., Gomperts, R., Stratmann, R. E., Yazyev, O. A., Austin, J., Cammi, R., Pomelli, C., Ochterski, J. W., Martin, R. L., Morokuma, K., Zakrzewski, V. G., Voth, G. A., Salvador, P., Dannenberg, J. J., Dapprich, S., Daniels, A. D., Farkas, O., Foresman, J. B., Ortiz, J. V., Cioslowski, J. & Fox, D. J. (2013). *GAUSSIAN 09*. Revision D. 01. Gaussian Inc., Wallingford, Connecticut, USA.
- Giordano, N., Afanasjevs, S., Beavers, C. M., Hobday, C. L., Kamenev, K. V., O'Bannon, E. F., Ruiz-Fuertes, J., Teat, S. J., Valiente, R. & Parsons, S. (2019). *Molecules*, **24**, 2018.
- Gonzalez-Platas, J., Alvaro, M., Nestola, F. & Angel, R. (2016). *J. Appl. Cryst.* **49**, 1377–1382.
- Grimme, S. (2006). *J. Comput. Chem.* **27**, 1787–1799.
- Grimme, S., Antony, J., Ehrlich, S. & Krieg, H. (2010). *J. Chem. Phys.* **132**, 154104.
- Groom, C. R., Bruno, I. J., Lightfoot, M. P. & Ward, S. C. (2016). *Acta Cryst.* **B72**, 171–179.
- Hahn, T., Janovec, V. & Klapper, H. (1999). *Ferroelectrics*, **222**, 11–21.
- Keith, T. A. (2019). *AIMAll*. Version 19.10.12. TK Gristmill Software, Overland Park, Kansas, USA.
- Krause, L., Herbst-Irmer, R., Sheldrick, G. M. & Stalke, D. (2015). *J. Appl. Cryst.* **48**, 3–10.

- Likhacheva, A. Y., Rashchenko, S. V., Chanyshv, A. D., Inerbaev, T. M., Litasov, K. D. & Kilin, D. S. (2014). *J. Chem. Phys.* **140**, 8.
- Macrae, C. F., Sovago, I., Cottrell, S. J., Galek, P. T. A., McCabe, P., Pidcock, E., Platings, M., Shields, G. P., Stevens, J. S., Towler, M. & Wood, P. A. (2020). *J. Appl. Cryst.* **53**, 266–235.
- Makhotkina, O., Lieffrig, J., Jeannin, O., Fourmigué, M., Aubert, E. & Espinosa, E. (2015). *Cryst. Growth Des.* **15**, 3464–3473.
- Marzouki, M. A., Souvignier, B. & Nespolo, M. (2014a). *IUCrJ*, **1**, 39–48.
- Marzouki, M. A., Souvignier, B. & Nespolo, M. (2014b). *Acta Cryst.* **A70**, 348–353.
- Marzouki, M.-A., Souvignier, B. & Nespolo, M. (2015). *Acta Cryst.* **A71**, 195–202.
- Mishra, A. K., Murli, C., Pandey, K. K., Sakuntala, T., Poswal, H. K. & Verma, A. K. (2020). *J. Phys. Chem. B*, **124**, 373–379.
- Momma, K. & Izumi, F. (2011). *J. Appl. Cryst.* **44**, 1272–1276.
- Murata, K., Yokogawa, K., Yoshino, H., Klotz, S., Munsch, P., Irizawa, A., Nishiyama, M., Iizuka, K., Nanba, T., Okada, T., Shiraga, Y. & Aoyama, S. (2008). *Rev. Sci. Instrum.* **79**, 085101.
- Nespolo, M. (2015). *Cryst. Res. Technol.* **50**, 362–371.
- Nespolo, M. (2019). *Acta Cryst.* **A75**, 551–573.
- Nespolo, M. & Aroyo, M. I. (2016). *Acta Cryst.* **A72**, 523–538.
- Nespolo, M. & Ferraris, G. (2007). *Acta Cryst.* **A63**, 278–286.
- Orgzall, I., Emmerling, F., Schulz, B. & Franco, O. (2008). *J. Phys. Condens. Matter*, **20**, 295206.
- Petitjean, M. (1994). *J. Comput. Chem.* **15**, 507–523.
- Piermarini, G. J., Block, S., Barnett, J. D. & Forman, R. A. (1975). *J. Appl. Phys.* **46**, 2774–2780.
- Pritchard, B. P., Altarawy, A., Didier, B., Gibson, T. D. & Windus, T. L. (2019). *J. Chem. Inf. Model.* **59**, 4814–4820.
- Putkonen, M.-L., Feld, R., Vettier, C. & Lehmann, M. S. (1985). *Acta Cryst.* **B41**, 77–79.
- Sheldrick, G. M. (2008). *Acta Cryst.* **A64**, 112–122.
- Sheldrick, G. M. (2015a). *Acta Cryst.* **A71**, 3–8.
- Sheldrick, G. M. (2015b). *Acta Cryst.* **C71**, 3–8.
- Sleboznick, C., Zhao, J., Angel, R., Hanson, B. E., Song, Y., Liu, Z. X. & Hemley, R. J. (2004). *Inorg. Chem.* **43**, 5245–5252.
- Tiekink, E. & Zukerman-Schpector, J. (2017). *Multi-Component Crystals, Synthesis, Concepts, Function*, Berlin, Boston: De Gruyter, xv+347 pp.
- Turner, M. J., McKinnon, J. J., Wolff, S. K., Grimwood, D. J., Spackman, P. R., Jayatilaka, D. & Spackman, M. A. (2017). *CrystalExplorer17*. University of Western Australia.
- Voute, A., Deutsch, M., Kalinko, A., Alabarse, F., Brubach, J.-B., Capitani, F., Chapuis, M., Ta Phuoc, V., Sopracase, R. & Roy, P. (2016). *Vibr. Spectrosc.* **86**, 17–23.
- Yan, T., Li, S., Wang, K., Tan, X., Jiang, Z., Yang, K., Liu, B., Zou, G. & Zou, B. (2012). *J. Phys. Chem. B*, **116**, 9796–9802.